

Supporting Information

Interphase structures and dynamics near nanofiller surfaces in polymer solutions

Tadanori Koga^{1,2,*}, Deborah Barkley², Michihiro Nagao^{3,4}, Takashi Taniguchi⁵, Jan-Michael Y. Carrillo⁶, Bobby G. Sumpter⁶, Tomomi Masui⁷, Hiroyuki Kishimoto⁷, Maho Koga⁸, Jonathan G. Rudick², Maya K. Endoh¹

¹Department of Materials Science and Chemical Engineering, Stony Brook University, Stony Brook, New York 11794-2275

²Department of Chemistry, Stony Brook University, Stony Brook, New York, 11794-3400

³NIST Center for Neutron Research, National Institute of Standards and Technology, Gaithersburg, Maryland, 20899-6102

⁴Center for Exploration of Energy and Matter, Indiana University, Bloomington, Indiana, 47408

⁵Graduate School of Engineering, Department of Chemical Engineering, Kyoto University, Katsura-Campus, Nishikyo-ku, Kyoto, 615-8510, Japan

⁶Center for Nanophase Materials Sciences and Computational Sciences and Engineering Division, Oak Ridge National Laboratory, Oak Ridge, Tennessee, 37831

⁷Sumitomo Rubber Industries Ltd., 1-1, 2-chome, Tsutsui-cho, Chuo-ku, Kobe, 671-0027, Japan

⁸Cornell University, Department of Biological and Environmental Engineering, Ithaca, New York, 14853

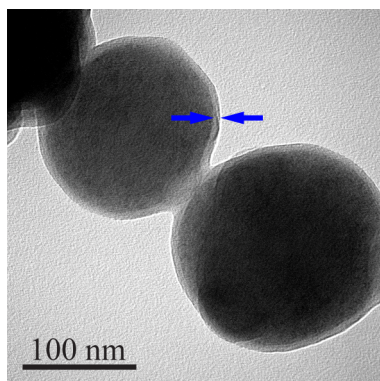


Figure S1. TEM image of the BPL-coated CB filler. The brighter region indicated by the arrows corresponds to the bound polymer layer. The data from Ref. 1.

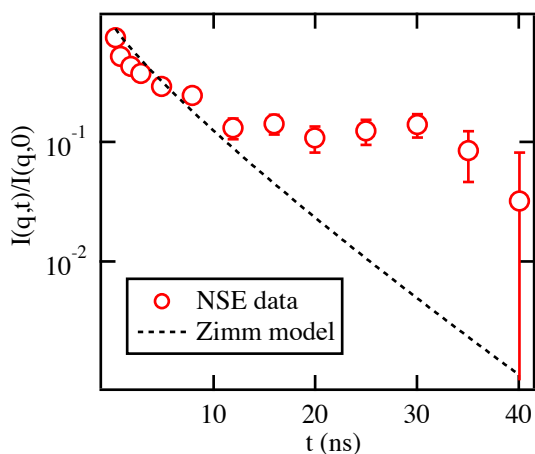


Figure S2. Measured $I(q,t)/I(q,0)$ (symbols) for the BPL(hPB35k)-coated CB in dPB115k/d-toluene at $c/c^* = 1.83$ at $q = 0.94 \text{ nm}^{-1}$ and calculated $I(q,t)/I(q,0)$ (dotted line) of the Zimm model². The viscosity of toluene (0.55 mPas at $25 \text{ }^\circ\text{C}$) was used for the calculation. Hence, it is clear that the overall dynamic structure factor cannot be described by the Zimm model.

Molecular Dynamics Simulations. We performed implicit solvent coarse-grained molecular dynamics simulation of polymer chains that are adsorbed in a highly adsorbing surface (representing carbon black) in a polymer solution matrix. The equilibrium conformation of adsorbed polymer chains should be dependent on spatial patterns of adsorption sites on a substrate, when pattern features and polymer sizes are comparable⁴. For example, Shu and co-workers previously studied polymer nanocomposites with textured nanoparticles, and found enhanced composition properties that were attributed to better interfacial adhesion due to the rough surface⁵. Their zeolite particles were 5 μm in size with surface features of about 50 nm in length. While the surface of the CB particles is not smooth but rough, characterized by surface fractal^{6, 7}, the characteristic surface feature of the individual filler (86 nm in the average diameter) is expected to be at the order of 1 nm^{8,9}, which is much smaller than the size of the polymer. We therefore assumed that the adsorbing surface is smooth, ignoring the effect of surface roughness on polymer adsorption. In addition, an internal inhomogeneous (i.e., turbostratic) structure of a CB filler, which is expected to be less than 1 nm¹⁰, can be considered as an impenetrable substrate.

The interaction between all beads is described by the truncated-shifted Lennard-Jones (LJ) potential,

$$U_{LJ}(r) = \begin{cases} 4\varepsilon_{LJ} \left[\left(\frac{\sigma}{r_{ij}} \right)^{12} - \left(\frac{\sigma}{r_{ij}} \right)^6 - \left(\frac{\sigma}{r_{cut}} \right)^{12} + \left(\frac{\sigma}{r_{cut}} \right)^6 \right] & r < r_{cut} \\ 0 & r \geq r_{cut} \end{cases} \quad (\text{S1})$$

where r_{ij} is the distance between the i^{th} and j^{th} bead, ε_{LJ} is the well depth. r_{cut} is the cutoff, which is equal to 2.5σ (where σ is the diameter of a Lennard-Jones bead) for monomer to substrate interactions (i.e., a short-ranged attractive substrate) and $2^{1/6}\sigma$ for monomer to monomer interactions (i.e., purely repulsive monomers or, in good solvent conditions for the monomers). The ε_{LJ} between monomer beads and between monomer and substrate beads are $1 k_B T$ and $8 k_B T$, respectively¹¹. The connectivity of monomers into polymer chains was maintained by the finite extension nonlinear elastic (FENE) potential¹²,

$$U_{FENE}(r) = -\frac{1}{2}k_s R_m^2 \ln \left(1 - \frac{r^2}{R_m^2} \right) \quad (\text{S2})$$

with the spring constant $k_s = 30.0 k_B T / \sigma^2$, and maximum bond length $R_m = 1.5\sigma$.

The interface between the surface and the adsorbed polymer matrix is at $z = 0$ and a repulsive bounding wall is located at L_z . The adsorbing surface is made up of 4 layers of Lennard-Jones beads arranged in a hexagonal closed packed lattice. First, we randomly placed the polymer with degree-of-polymerization (N_{BPL}) in contact with a highly adsorbing substrate and compressed the simulation box by moving the top bounding wall to attain intimate contact with the substrate (see step 1 in Fig. S3). The compression was done slowly and proceeded up to $10^5 \tau$. Here, τ is the characteristic time defined as $\tau = \sigma(m/k_B T)^{1/2}$ (m is the mass of a bead and $k_B T$ is the thermal energy). Second, we released the compression by moving back the top wall to the top of the simulation box, allowing the simulation to proceed to attain the equilibrium number of adsorbed chains and their respective chain conformations (see step 2 in Fig. S3). This step proceeded up to $10^5 \tau$. Third, we removed all unadsorbed chains, similar to a rinsing step, and retained the

adsorbed chains, which we identified as the bound polymer layer or BPL. An adsorbed chain is defined as a chain where one of its beads is within 1.18σ from a substrate bead (see step 3 in Fig. S3). This step lasted for $2 \times 10^4 \tau$. Fourth, we introduced the polymer solution by adding m_{free} chains at different polymer concentrations (c), and degrees-of-polymerization (N_{free}), and allowed the free chains to equilibrate for $10^4 \tau$ (see step 4 in Fig. S3). Afterwards, we performed production simulation runs which proceeded up to $10^5 \tau$.

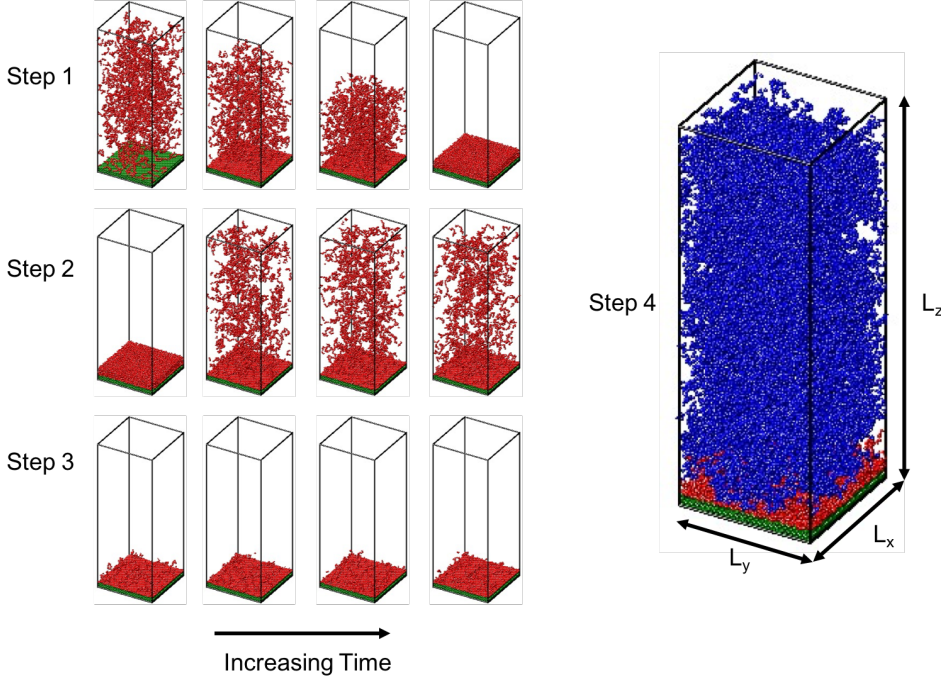


Figure S3. Equilibration simulation steps: (1) Adsorption of polymers (red beads) to a highly adsorbing substrate (green beads) aided by compressing the top wall (not shown). (2) Release of top-wall and desorption of weakly adsorbed chains. (3) Removal of unadsorbed chains and equilibration of the bound polymer layer. (4) Addition of polymer chains (blue beads) at polymer concentration, c , in a simulation box with dimensions $L_x=40\sigma$, $L_y=39.84\sigma$, and $L_z=(m_{\text{free}}N_{\text{free}})/(cL_xL_y)$.

The simulations were carried out at a constant number of particles and temperature ensemble (canonical or NVT ensemble). The constant temperature was maintained by coupling the system to a Langevin thermostat implemented in LAMMPS^{13,14}. In this case, the equation of motion of the i^{th} particle is

$$m \frac{d\vec{v}_i(t)}{dt} = \vec{F}_i(t) - \xi_L \vec{v}_i(t) + \vec{F}_i^R(t) \quad (\text{S3})$$

where $\vec{v}_i(t)$ is the bead velocity and $\vec{F}_i(t)$ is the net deterministic force acting on the bead with mass m , which was kept constant for all particles. $\vec{F}_i^R(t)$ is the Gaussian stochastic force with zero average value $\langle \vec{F}_i^R(t) \rangle = 0$ and variance $\langle \vec{F}_i^R(t) \vec{F}_j^R(t') \rangle = 6\delta_{ij}\xi_L k_B T \delta(t - t')$. The friction coefficient is set to $\xi_L = 1/7 m/\tau$ and the thermal energy scale, $k_B T$, is set to 1.0. The velocity-Verlet algorithm with a time step of 0.01τ was used for time integration. The substrate beads are excluded from the integration, thus, freezing the substrate.

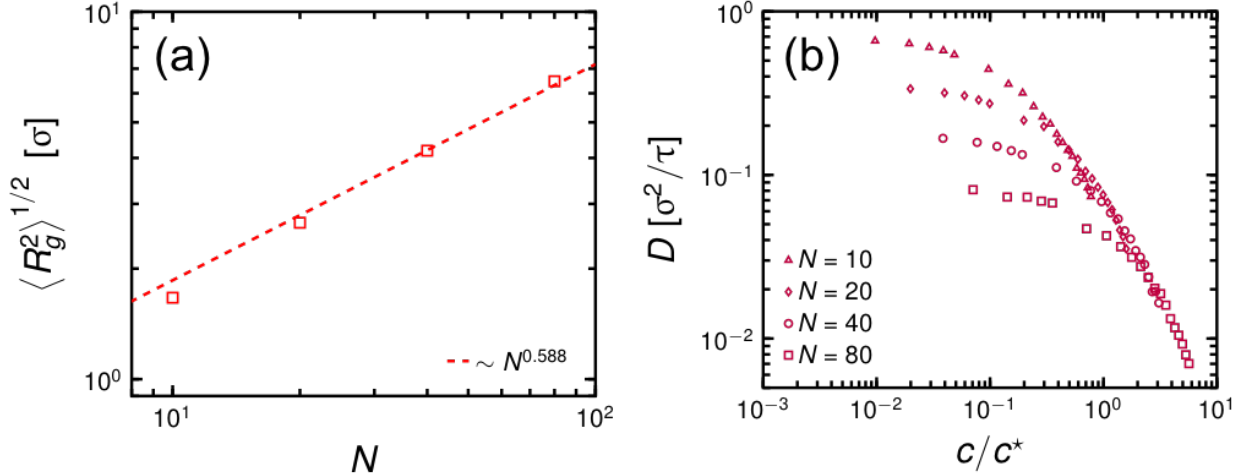


Figure S4. Dependence of chain radius of gyration, $\langle R_g^2 \rangle^{1/2}$ as a function of degree-of-polymerization, N , obtained from simulations of single polymer chains (a). The dashed line is a power law with exponent 0.588, representing good solvent quality for the polymers.¹⁵ Dependence of chain center-of-mass diffusion coefficient, D , as a function of the ratio of the polymer concentration with overlap concentration, c/c^* for chains with different degrees-of-polymerization, N .

To obtain the overlap concentration, c^* , we performed single-chain implicit solvent simulations at the dilute limit at different degrees-of-polymerization, N , and having the same simulation parameters described above, but without the attractive substrate. We define c^* as $c^* = 3N/4\pi\langle R_g^2 \rangle^{3/2}$ ¹⁵, or as the polymer concentration of the spherical volume pervaded by an unperturbed chain's radius of gyration, $\langle R_g^2 \rangle^{1/2}$. Next, we proceed running multi-chain simulations to obtain the dependence of the long-time center-of-mass diffusion coefficient, D , with polymer concentration, c , where $D = \lim_{t \rightarrow \infty} \langle \delta \vec{r}^2(t) \rangle / 6t$, is obtained from the mean-square displacement (MSD), $\delta \vec{r}^2(t)$ of the chain center-of-mass.

For the production runs of the systems having a highly attractive substrate (green beads in Figs. S5(a) and (b)), the different types of polymers are classified as follows: (1) the bound polymer layer are made up of polymers that are in contact with the highly adsorbed substrate (red beads in Figs. S5(a) and (b)), (2) the interacting polymer chains are the polymers that are in direct contact with the polymer chains in the bound polymer layer (cyan beads in Fig. S5(b)), and (3) the free polymers or the chains that are not in direct contact with the bound polymer layer (blue dots in Fig. S5(b)). Hence, the polymer solution (blue beads in Fig. S5(a)) is composed of both the interacting and free chains. A chain is in contact with the bound polymer layer if one of its beads is located within 1.18σ of any bead belonging to a bound polymer layer chain.

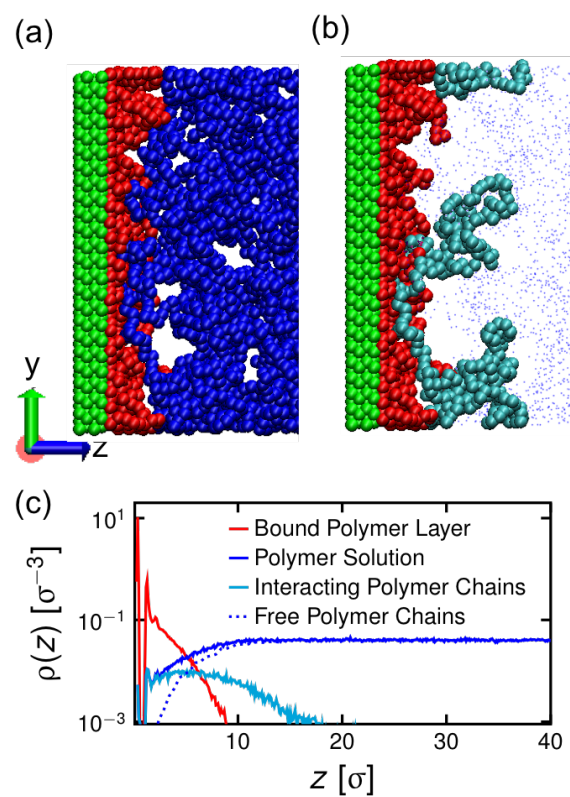


Figure S5. Snapshot of the simulation with a highly attractive substrate. The substrate is shown as green beads in (a) and (b), the bound polymer layer as red beads in (a) and (b), and the polymer solution is shown as blue beads in (a), which are further categorized as interacting polymer chains, which are the cyan beads in (b), and free polymer chains, which are the blue dots in (b). The monomer density distribution of each polymer bead-type is shown in (c).

Unified approach for the SANS results

In order to analyze the structures of the CB fillers, we utilized the unified equation¹⁶:

$$I(q) = A \exp\left(-\frac{q^2 R_{g,BR}^2}{3}\right) q^{-\alpha} + B \exp\left(-\frac{q^2 R_{g,BR}^2}{3}\right) + C \left[\operatorname{erf}\left(\frac{q R_{g,BR}}{\sqrt{6}}\right)\right]^3 / q \exp(-\sigma^2 q^2), \quad (\text{S4})$$

where $R_{g,BR}$ is the radius of gyration of the entire BPL-coated CB fillers, and α , β , A , B , C are numerical constants. The first term in the rhs of eq. (S4) represents power-law scattering profile. The exponential prefactor of $q^{-\alpha}$ serves as a damping factor for the power-law at $qR_{g,BR} > 1$. Since the q -range is limited, we used the power exponent of -2.1 based on the previous USANS results for the BPL-coated CB fillers¹. The second term in the rhs of eq. (S4) represents the Guinier scattering for the entire BPL-coated CB filler with $R_{g,BR}$. The third term of the rhs of eq. (S4) represents the power-law scattering profile with the upper cut-off length $R_{g,BR}$; the term $[\operatorname{erf}(qR_{g,BR}/\sqrt{6})]^{3\beta}$ serves as a damping factor for the power-law at the small q -range at $qR_{g,BR} \leq 1$. According to a previous combined small-angle scattering study¹⁷, CB filled elastomers exhibited power law scattering of $q^{-3.4}$ at the high q regime, while the pure CB fillers themselves showed power-law scattering of $q^{-3.6}$. The difference in the power exponent indicates the existence of a bound rubber layer on the filler surface embedded in the elastomer matrices. While the CB grade and matrix polymer used in this study are different from those used for the previous study, we assumed the power exponent to be -3.4 to express the BPL-coated CB surface. The interfacial root-mean-square roughness (σ) between the BPL-coated CB and d-toluene was independently determined to be 2.3 nm¹. The $R_{g,BR}$ values of the BPL(hPB35k)-coated CB fillers and the BPL(hPB115k)-coated CB filler were determined to be (57 ± 5) nm and (60 ± 5) nm, respectively, based on the best-fits of the unified equation to the SANS profiles.

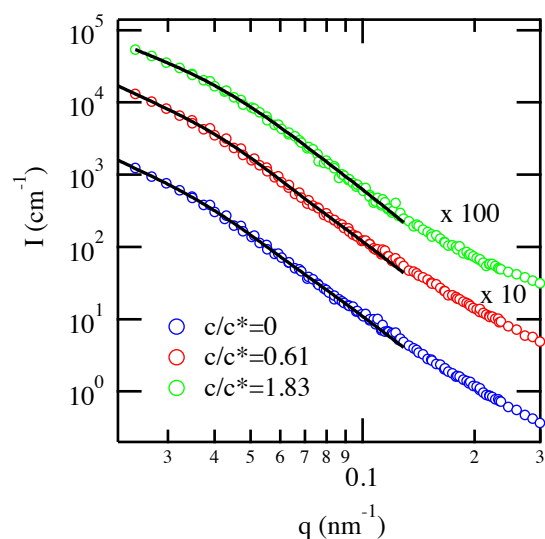


Figure S6. SANS profile of the BPL (hPB115k)-coated CB fillers in dPB115/d-toluene solution. Note the incoherent scattering intensity is subtracted from the data. The solid lines correspond to the best-fits of eq. (S4) to the SANS data.

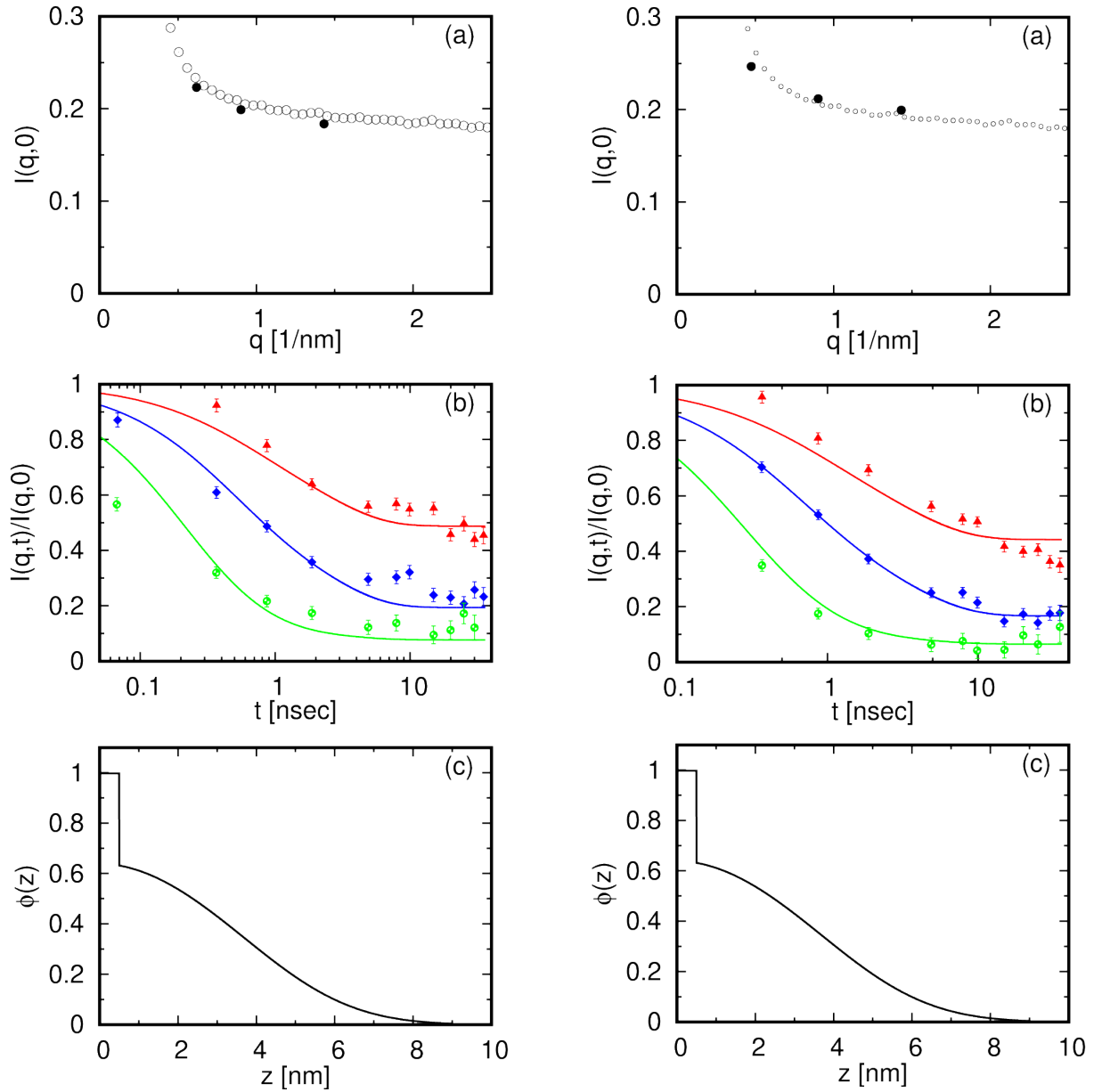


Figure S7. Fitting results for the BPL(hPB35k)-coated CB in the dPB115k/d-toluene at the three different q values ($q=0.65$ (red), 0.94 (blue) and 1.47 (green) nm^{-1}) for (I) $c/c^*=0$ (left column) and (II) $c/c^*=0.61$ (right column): (a) Excess scattering (open symbols, $I(q,0)$) after subtraction of the filler scattering calculated by eq. (S4). The closed circles represent the calculated $I(q,0)$ at the three different q values used, which corresponds to the denominator of the right hand side of eq. (3). (b) Measured $I(q,t)/I(q,0)$ (symbols). The error bars represent ± 1 standard deviation. The solid lines correspond to the best-fits of the breathing model (eq. (3)). (c) the volume fraction profile of the BPL vs. the distance (z) from the CB surface obtained from the best-fits of the breathing model.

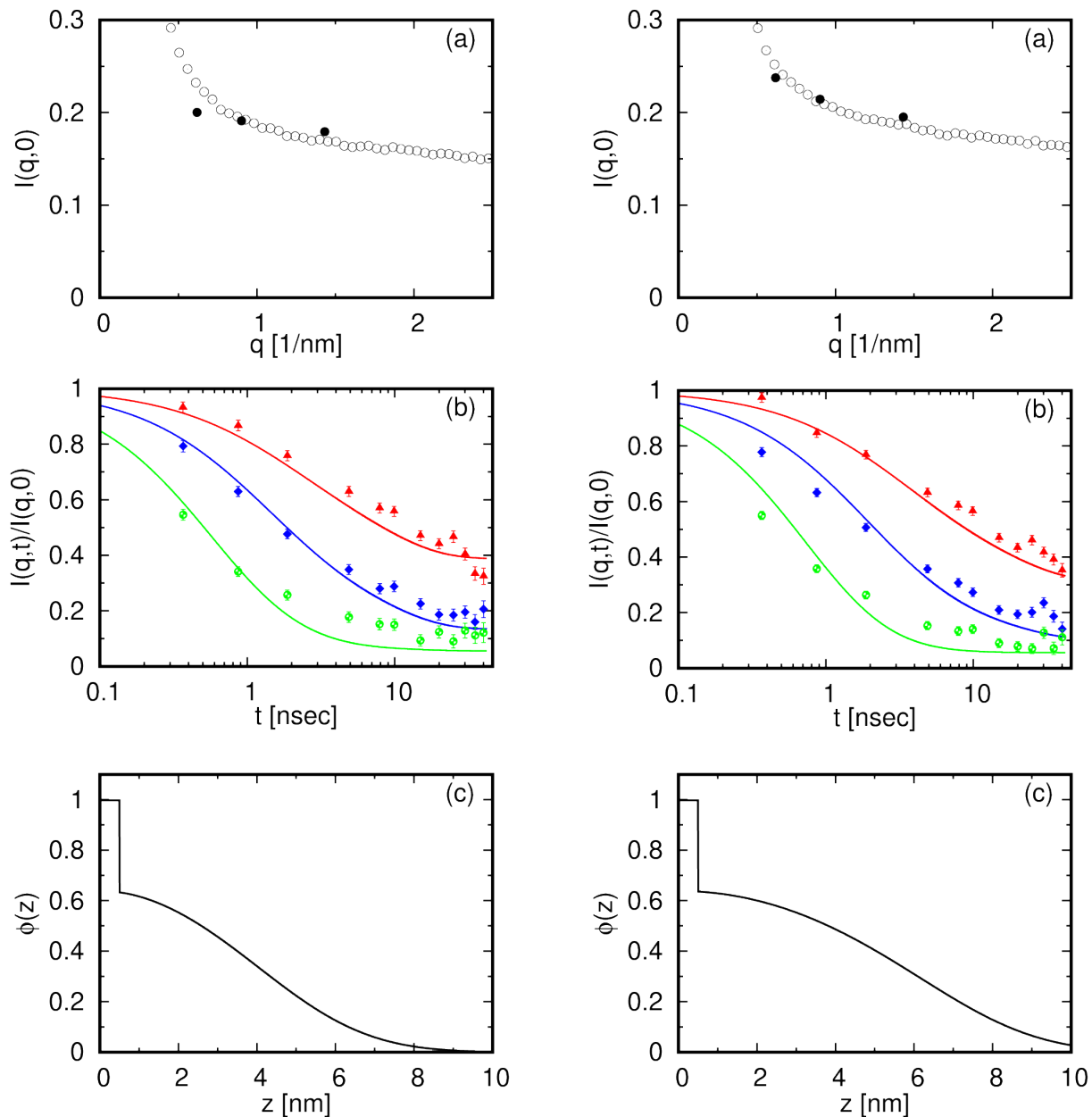


Figure S8. NSE and SANS fitting results for the BPL(hPB35k)-coated CB in dPB35k/d-toluene (left column) and for the BPL(hPB115k)-coated CB in dPB115k/d-toluene (right column) at for $c/c^*=0.61$: (a) Excess scattering (open symbols, $I(q,0)$) after subtraction of the filler scattering calculated by eq. (S4). The closed circles represent the calculated $I(q,0)$ at the three different q values used for the fitting shown in (b). (b) Measured $I(q,t)/I(q,0)$ (symbols) at the three different q values ($q=0.62$ (red), 0.90 (blue) and 1.43 (green) nm⁻¹). The error bars represent ± 1 standard deviation. The solid lines correspond to the best-fits of the breathing model (eq. (3)). (c) the volume fraction profile of the BPL vs. the distance (z) from the CB surface obtained from the best-fits of the breathing model.

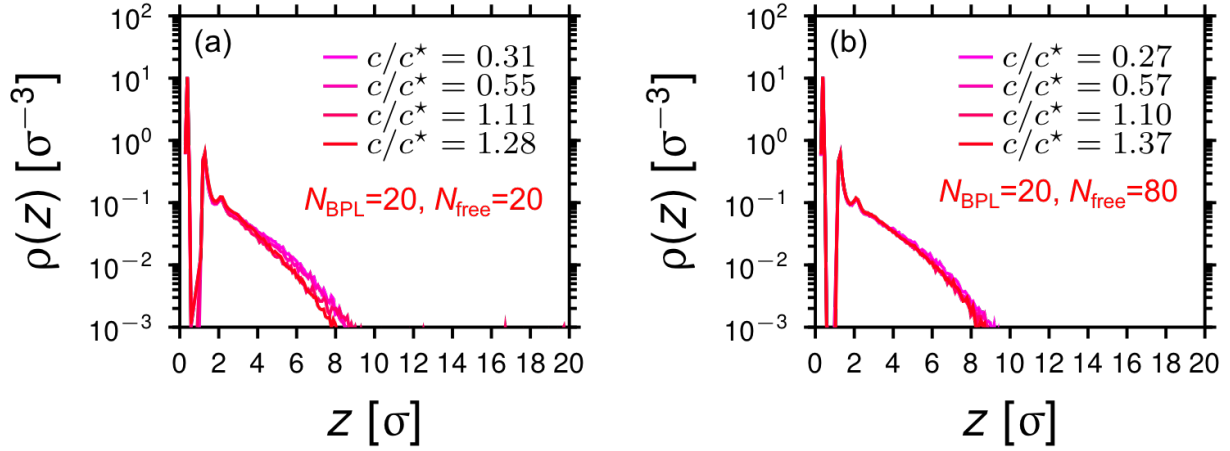


Figure S9. Monomer density distribution of the bound polymer layer for systems with $N_{\text{BPL}}=20$ and $N_{\text{free}}=20$ (a) and $N_{\text{free}}=80$ (b) at different values of c/c^* . Note that the beads (1σ in size) form a monolayer after completely coating the substrate. The dip around 1σ is hence the boundary between the first coating and the next layer.

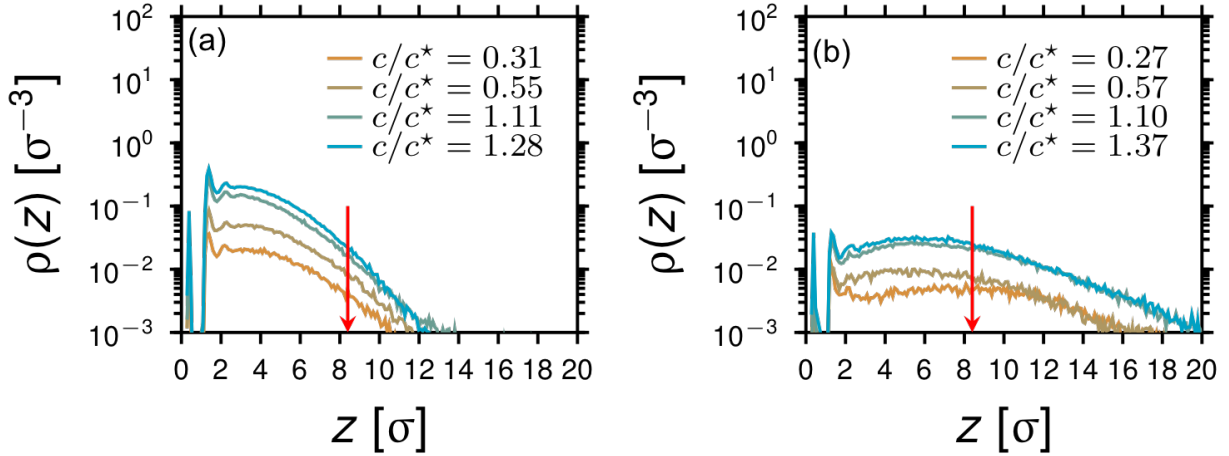


Figure S10. Monomer density distribution of the interacting polymer chains for systems with $N_{\text{BPL}}=20$ and $N_{\text{free}}=20$ (a) and $N_{\text{free}}=80$ (b) at different values of c/c^* . The red arrows mark the extent of the bound polymer layer.

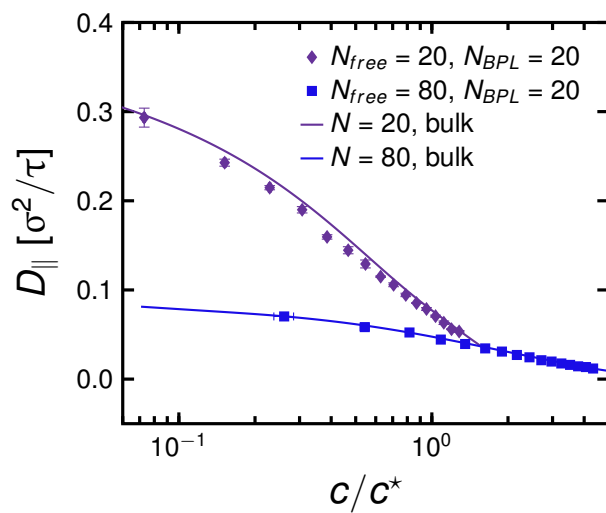


Figure S11. Diffusion coefficients parallel to the substrate, D_{\parallel} , as a function of c/c^* of the free polymer chains.

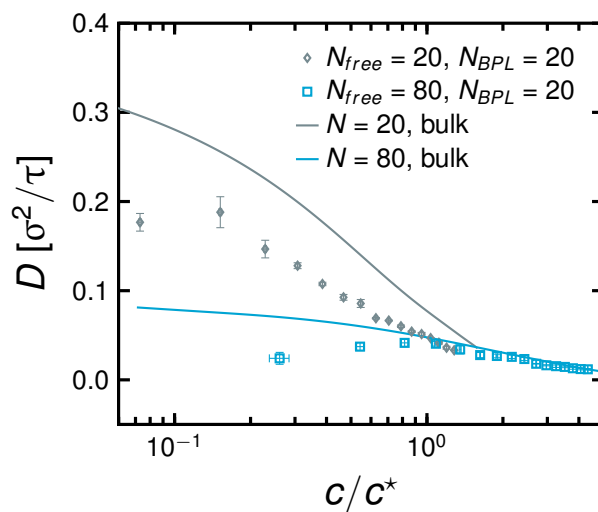


Figure S12. Diffusion coefficients of D as a function of c/c^* of the interacting polymer chains.

SANS data analysis

To estimate the incoherent scattering, we used the method proposed for various types of hydrogen-containing materials¹⁸. According to the method, a differential incoherent scattering cross section of a sample at the zero-thickness limit $((d\Sigma/d\Omega)_{inc})$ is given by

$$(d\Sigma/d\Omega)_{inc} \cong \frac{1}{4\pi} \frac{1-T}{tT}, \quad (S5)$$

where t and T are the thickness of the sample and the sample transmission, respectively. We measured the transmission of each sample (2 mm in thickness) that was contained in a custom-made titanium cell with quartz windows. We used this calculated value as a constant incoherent scattering contribution for the entire q -range.

References

1. Jiang, N.; Endoh, M. K.; Koga, T.; Masui, T.; Kishimoto, H.; Nagao, M.; Satija, S. K.; Taniguchi, T. Nanostructures and Dynamics of Macromolecules Bound to Attractive Filler Surfaces, *ACS Macro Lett.* **2015**, *4*, 838-842.
2. Richter, D.; Monkenbusch, M.; Arbe, A.; Colmenero J., Neutron Spin Echo in Polymer Systems, *Adv. Polym. Sci.*, **2005**, *174*, 1-221.
3. Santos, F. J. V. ; Nieto de Castro, C. A.; Dymond, J. H.; Dalaouti, N. K.; Assael, M. J.; Nagashima, A. Standard Reference Data for the Viscosity of Toluene, *J. Phys. Chem. Ref. Data*, **2006**, *35*, 1-8,
4. Venkatakrishnan, A.; Kuppa, V. K. Polymer adsorption on rough surfaces, *Curr. Opin. Chem. Eng.* **2018**, *19*, 170-177.
5. Shu, S.; Husain, S.; Koros, W. J. A General Strategy for Adhesion Enhancement in Polymeric Composites by Formation of Nanostructured Particle Surfaces, *J. Phys. Chem. C* **2007**, *111*, 652-657.
6. Rieker, T. P.; Hindermann-Bischoff, M.; Ehrburger-Dolle, F. Small-Angle X-ray Scattering Study of the Morphology of Carbon Black Mass Fractal Aggregates in Polymeric Composites, *Langmuir* **2000**, *16*, 5588-5592.
7. Koga, T.; Hashimoto, T.; Takenaka, M.; Aizawa, K.; Amino, N.; Nakamura, M.; Yamaguchi, D.; Koizumi, S. New insight into hierarchical structures of carbon black dispersed in polymer matrices: A combined small-angle scattering study, *Macromolecules* **2008**, *41*, 453-464.
8. Raab, H.; Frohlich, J.; Regensburg, D. G. Surface Topography and its Influence on the Activity of Carbon Black, *KGK-Kaut. Gummi Kunst.* **2000**, *53*, 137-143.
9. Niedermeier, W.; Raab, H.; Stierstorfer, J.; Kreitmeier, S.; Regensburg, D. G. The Microstructure of Carbon Black Investigated by Atomic Force Microscopy, *KGK-Kaut. Gummi Kunst.* **1989**, *94*, 799-805.
10. Speck, J. S.; Endo, M.; Dresselhaus, M. S. Structure and intercalation of thin benzene derived carbon fibers, *J. Cryst. Growth* **1989**, *94*, 834-848.
11. Carrillo, J. M. Y.; Cheng, S. W.; Kumar, R.; Goswami, M.; Sokolov, A. P.; Sumpter, B. G. Untangling the Effects of Chain Rigidity on the Structure and Dynamics of Strongly Adsorbed Polymer Melts, *Macromolecules* **2015**, *48*, 4207-4219.
12. Kremer, K.; Grest, G. S. Dynamics of Entangled Linear Polymer Melts - a Molecular-Dynamics Simulation, *J. Chem. Phys.* **1990**, *92*, 5057-5086.
13. Plimpton, S. J. Fast parallel algorithms for short-range molecular dynamics, *J. Comput. Phys.* **1995**, *117*, 1-19.
14. Brown, W. M.; Wang, P.; Plimpton, S. J.; Tharrington, A. N. Implementing molecular dynamics on hybrid high performance computers—short range forces, *Comput. Phys. Commun.* **2011**, *182*, 898-911.
15. Rubinstein, M.; Colby, R. H., *Polymer Physics*. Oxford University Press: 2003.
16. Beaucage, G. Approximations Leading to a Unified Exponential/Power -Law Approach to Small-Angle Scattering, *J. Appl. Cryst.* **1995**, *28*, 717-728.
17. Koga, T.; Hashimoto, T.; Takenaka, M.; Aizawa, K.; Amino, N.; Nakamura, M.; Yamaguchi, D.; Koizumi, S. New Insight into Hierarchical Structures of Carbon Black Dispersed in Polymer Matrices: A Combined Small-angle Scattering Study, *Macromolecules* **2008**, *41*, 453-464.
18. Shibayama M.; Matsunaga T.; Nagao. M., Evaluation of incoherent scattering intensity by transmission and sample thickness *J. Appl. Cryst.* **2009**, *42*, 621–628